Clinical Validation of a Three-Dimensional Ultrafast Cardiac Magnetic Resonance Protocol Including Single Breath-Hold Three-Dimensional Sequences

ONLINE APPENDIX

SUPPLEMENTAL METHODS

The ESSOS reconstruction is based on the acquisition of two interleaved datasets, one static and other dynamic (**Supplemental Figure 1**). The static dataset (**Supplemental Figure 1a**) is acquired with a relatively low SENSE factor (S_{Static}) and is acquired only once in the cardiac cycle since it does not require any temporal information (in the example of Supplemental Figure 2, S_{Static} =3x2 in an extended FOV in AP direction to reach the nominal SENSE factor of 3x1.5). The dynamic (cine) dataset is acquired a with higher SENSE factor, S_{Dyn}, for each acquired heart phase (S_{Dyn}=24 in the example in **Supplemental Figure 1b**). ESSOS subtracts the signal from the outer static image regions (static dataset) (**Supplemental Figure 1c**) from the dynamic dataset. The reconstructed FOV of the dynamic dataset can now be reduced to a smaller "dynamic FOV" (inner region Supplemental Figure 2c), which proportionately lowers the corresponding SENSE factor. This allows ESSOS to use a S_{Dyn} higher than the maximum factor that can be applied with conventional SENSE.

The ESSOS reconstruction is divided into three blocks (**Supplemental Figure 2**): static information preparation, static information removal from the dynamic dataset, and dynamic reconstruction.

<u>Static information preparation (Supplemental Figure 2a)</u>

The subtraction of the static region signal from the dynamic dataset needs to be performed on a coil-by-coil basis in k-space. In order to match the data from each coil element in the dynamic dataset, subtraction needs to be preceded by coil weighting and subsampling on the unwrapped images of the static dataset.

To obtain the individual unwrapped images for each coil element, the ESSOS reconstruction begins by applying the conventional SENSE reconstruction to the static dataset (Step 1, **Supplemental Figure 2a**), which provides an image corrected for the varying coil sensitivities. For each coil element, this image is then multiplied by the coil sensitivity (Step 2, **Supplemental Figure 2a**).

The dynamic region is then defined and nulled by setting the pixels inside the dynamic region to zero (Step 3, **Supplemental Figure 2a**) and leaving static regions with the original signal. To illustrate the method, the dynamic region is defined in **Supplemental Figure 2** as a rectangle in the center of the Y-Z FOV and with an area 4 times smaller than the entire FOV (2 times smaller in the AP and the LR directions). The dynamic region does not have to be rectangular, and can have any shape.

The resulting masked and weighted synthetic data are subsequently Fourier transformed to k-space (for each coil element) and then subsampled using the same sampling pattern used in the second (dynamic) dataset (Step 4, **Supplemental Figure 2a**).

<u>Removal of static information from the dynamic dataset (Supplemental Figure 2b)</u>

The signal in the static region is assumed to be constant during the cardiac cycle and can be eliminated by subtracting the synthesized static data generated in Step 4 from each cardiac phase and coil element of the second dynamic dataset (Step 5, **Supplemental Figure 2b**). The net result of Step 5 is that the outer (static) part of the FOV is removed from the dynamic dataset, leaving only the inner (dynamic) part of the FOV. This significantly reduces the

amount of aliasing in the dynamic dataset to be used as input for subsequent SENSE reconstruction.

Dynamic reconstruction (Supplemental Figure 2c)

After the subtraction, the synthetic dynamic data only contains information from the smaller dynamic FOV, allowing SENSE reconstruction with a smaller SENSE factor, S^*_{Dyn} (Step 6, **Supplemental Figure 2c**). This reduction in the effective SENSE factor decreases the geometry factor and therefore noise amplification inside the dynamic region. On the other hand, the subtraction intrinsically increases the noise level, and any inaccuracy in the static image produces only partial suppression of the static tissue, consequently generating artefacts and noise amplification in the dynamic region.

The effective net undersampling factor S^*_{Dyn} within the dynamic FOV is defined as

$$S^*_{Dyn} = S_{Dyn} \frac{AFOV_{Dyn}}{AFOV}, \qquad \text{Eq. 1}$$

where $AFOV$ represents the area of the entire *FOV*, whereas $AFOV_{Dyn}$ is the area of the dynamic FOV. S^*_{Dyn} can be freely chosen so long as $S^*_{Dyn} \leq S_{Dyn}$, and the dynamic object of interest is enclosed by the dynamic FOV. In the example in **Supplemental Figure 2**, the area of the dynamic FOV is 4 times smaller than the entire FOV, proportionally lowering the effective SENSE factor (S^*_{Dyn}) ×4, from 24 to 6 (from 6x4 in the entire FOV to 3x2 in the dynamic FOV, LRxAP). This necessarily also lowers the maximal geometry-factor (g-factor) and noise amplification. Using the same dataset, multiple ESSOS reconstructions with different S^*_{Dyn} factors can be made by selecting different areas for the FOV_{Dyn} (Step 3, **Supplemental Figure 2a**). Note that for very small dynamic FOVs, S^*_{Dyn} can become 1x1, resulting in an even lower g-factor (this is done in the example of Supplemental Figure 3 by reducing the dynamic FOV to a quarter-size in the LR direction and half-size in the AP direction). The

minimum size for the dynamic FOV is limited by the need to fully contain the dynamic object and is not restricted to any particular shape.

Finally, after the SENSE reconstruction of the inner, dynamic FOV, the outer (static) part of the FOV is added to it to recover the entire FOV (static+dynamic). This step is not shown in Supplemental Figure 2.

Definition of Static-Dynamic Regions

In the previous section, the dynamic region was defined as a rectangular shape to simplify the illustration of ESSOS reconstruction. However, the dynamic region can have any shape, based on anatomical landmarks (manual contours) or assigned automatically based on the temporal information in the dynamic dataset. This irregularly shaped dynamic region is still referred to as the dynamic FOV. One way of defining the dynamic region would be to estimate the signal difference between each cardiac phase. A faster alternative is to analyze the temporal frequencies of the dynamic dataset by means of Fourier transformation in the temporal domain. In principle, this allows extraction by conventional SENSE of any locations with non-zero temporal frequency components, which correspond to the dynamic region (**Supplemental Figure 3**). Conventional SENSE can be applied directly with S_{Dyn} for the non-zero temporal frequency components because the effective SENSE factor is lower because these non-zero components are, by definition, only present in the smaller dynamic region.

Before applying SENSE, the number of frequency components is reduced by adding all positive frequencies to one dataset and all negative frequencies to a second dataset. Both datasets were reconstructed using conventional SENSE with an acceleration factor S_{Dyn} (**Supplemental Figure 3b**). Positive and negative components were processed separately to avoid potential cancelation of certain frequency components. The modulus of both datasets was added (**Supplemental Figure 3c**). Finally, the volume was segmented by thresholding in a dynamic region and a static region, and the result was cleaned by applying morphological

operations (dilatation and erosion). The resulting mask (**Supplemental Figure 3d**) was used to null the dynamic region (Step 3, **Supplemental Figure 2a**) in the static data. To minimize noise amplification during SENSE reconstruction, the mask was also used to null the coil sensitivity maps outside the dynamic region (feed forward regularization) before applying conventional SENSE with factor S_{Dyn} (1).

To evaluate the noise amplification improvement of ESSOS compared to regular SENSE in **Supplemental Figure 4** is presented a set of experiment using fully-sampled cine images. These images were acquired from a single axial slice located at the heart level in a single breath-hold using 2D-SSFP (TR/TE/FA= 2.7ms/1.34ms/40^{o}) covering a FOV of 380x330mm (LRxAP), 1.6x2.0mm in-plane voxel size, 8mm slice thickness and retrospectively cardiac triggering (25 cardiac phases). The fully sampled k-space was subsampled in two directions in order to simulate 3D accelerated acquisitions with SENSE and ESSOS (the frequency encoding direction of the 2D experiments was treated as a second phase encoding direction). For all the analysis fully sampled images were use as gold standard to compute error images and signal to noise ratio (SNR).

Error images were generated subtracting the full sampling images to the accelerated images reconstructed with SENSE and ESSOS for all cardiac phases and acceleration factors. For better visualization in **Supplemental Figure 4** the modulus images are presented. G-factor maps where also computed for SENSE and ESSOS for better comparison between both techniques. For ESSOS, two g-maps were generated for static and dynamic FOV applying corresponding feedforward regularization (13). Final ESSOS g-maps were obtained by multiplication of both g-maps.

Sample size calculation

Sample-size calculation was based on LVEF results obtained from a series of experiments performed in a large animal (pig) model of MI using 2D and 3D CMR imaging (data not shown). The calculation assumed a standard deviation for the difference in LVEF of 2% and a 95% confidence interval (CI) of +/- 5% for the limits of agreement between 2D and 3D cine imaging. This resulted in a sample size of 110 with a statistical power of 80% (MedCalc Software, Ostend, Belgium).

Absolute-agreement and consistency-of-agreement ICC values and their 95%CI were calculated using the *icc* command for two-way random-effects model for individual (single) measurements, except for LV wall thickening analysis in which correlation between average measurements was considered. Agreement was considered poor, moderate, good, or excellent for ICC values <0.50, 0.50-0.75, 0.75-0.90, and >0.90, respectively (2).

Bland-Altman analysis and plots were generated using the user-written *agree* command with the *ba* option. No significant systematic bias was assumed if the 95%CI for the mean between-measurement difference contained the value 0 (3). Limits of agreement were calculated on the assumption that between-measurement differences were normally distributed and included 95% of differences between the two measurements (±1.96 times the standard deviation of the mean difference). The underlying assumption of normal distribution was checked by visual inspection of the normal probability plots and tests of normality (Shapiro-Wilk and Kolmogorov-Smirnov) for the differences between compared results.

Passing-Bablok regression analysis and plots were generated using the *agree* command with the *pb* option. There was assumed to be no constant bias between measurements if the 95%CI of the intercept included the value 0, whereas an absence of significant proportional bias was assumed if the 95%CI of the intercept included the value 1 (4). Assuming normal distribution, 95% of random differences (or residuals) were expected to lie within ± 1.96 times

the residual standard deviation. The linear relationship between compared results was assessed by the CUSUM test for deviation of linearity.

Lin's concordance correlation coefficients were computed using the user-written *concord* command. This contains a measure of precision (Pearson's ρ) and accuracy (bias corrected factor) to determine how far the observed data deviate from the line of perfect concordance or agreement (i.e., the line at 45 degrees on a square scatter plot) (5). Because the interpretation is very similar, the same threshold values were used for Lin's concordance correlation coefficients as for ICC.

SUPPLEMENTAL FIGURES

Supplemental Figure 1. Schematic datasets, acquisition, and definition of FOV regions. **a, b)** Sampling scheme for acquisition of the static and dynamic datasets, as required for ESSOS. Dots represent ky and kz profiles for the corresponding frequency encoding acquisition (kx) in 3D k-space. Black and white dots represent acquired and non-acquired profiles, respectively. First dataset is constructed combined the information of four different cardiac phases acquired in diastole with shifted sampling pattern. Second dataset is obtained after temporal interpolation of the three cardiac used to build the first dataset. c) Axial (reformatted) view of 3D coronal volume, showing the definition of the (outer) static region (marked area) and the (inner) dynamic region.

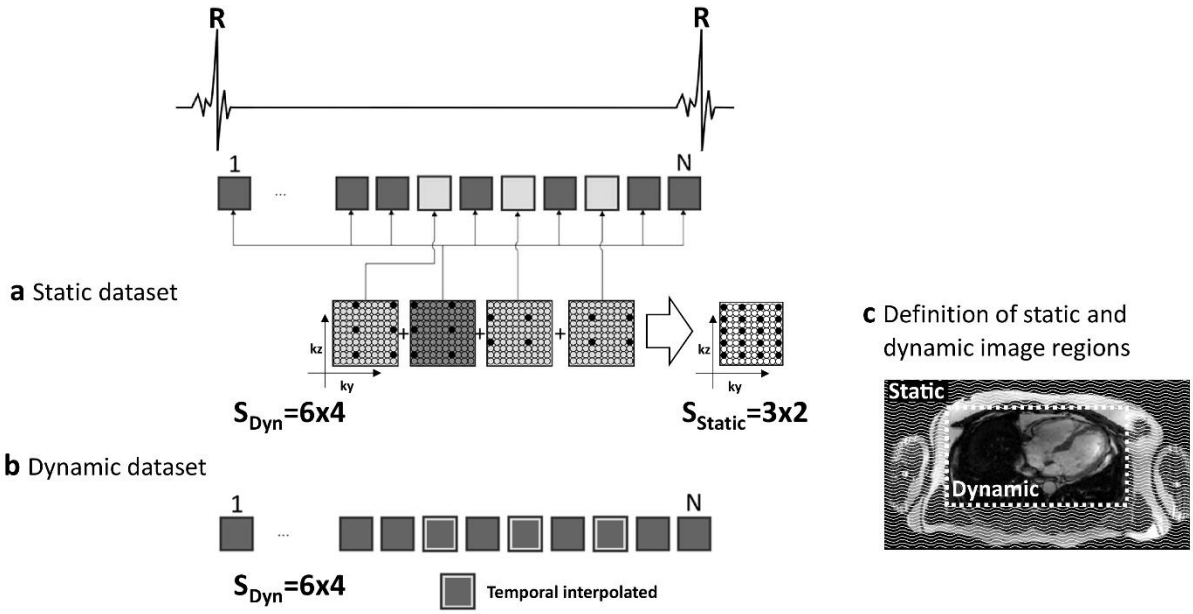

Supplemental Figure 2. ESSOS reconstruction scheme. Schematic representation of the three components of ESSOS reconstruction: **a)** Static information preparation. **b)** Static information removal (from the dynamic data). **c)** Dynamic reconstruction. Each block shows the results of the intermediate steps followed during ESSOS reconstruction. All images show axial reformats of a coronal 3D volume acquisition. Step 1, Conventional SENSE reconstruction of the large "static" FOV. Step 2, The "static" volumetric data is multiplied by the coil sensitivities: left, coil sensitivity maps; right, result after multiplication. Step 3, The inner (dynamic) part of the "static" data is masked out (set to zero) for each coil dataset. Step 4, The masked "static" dataset is Fourier transformed and synthetically subsampled with the same undersampling scheme as the "dynamic" dataset. Note that the k-space data from Step 4 and Step 5 are shown in the figure after inverse Fourier transformation (IFT) for better visualization. Step 5, The masked, subsampled "static" data from Step 4 (middle row in Step 5) are subtracted from the "dynamic" dataset (top row Step 5) on a coil-by-coil basis (bottom row Step 5). Step 6, The result from step 5 is reconstructed with SENSE in the smaller, dynamic FOV.

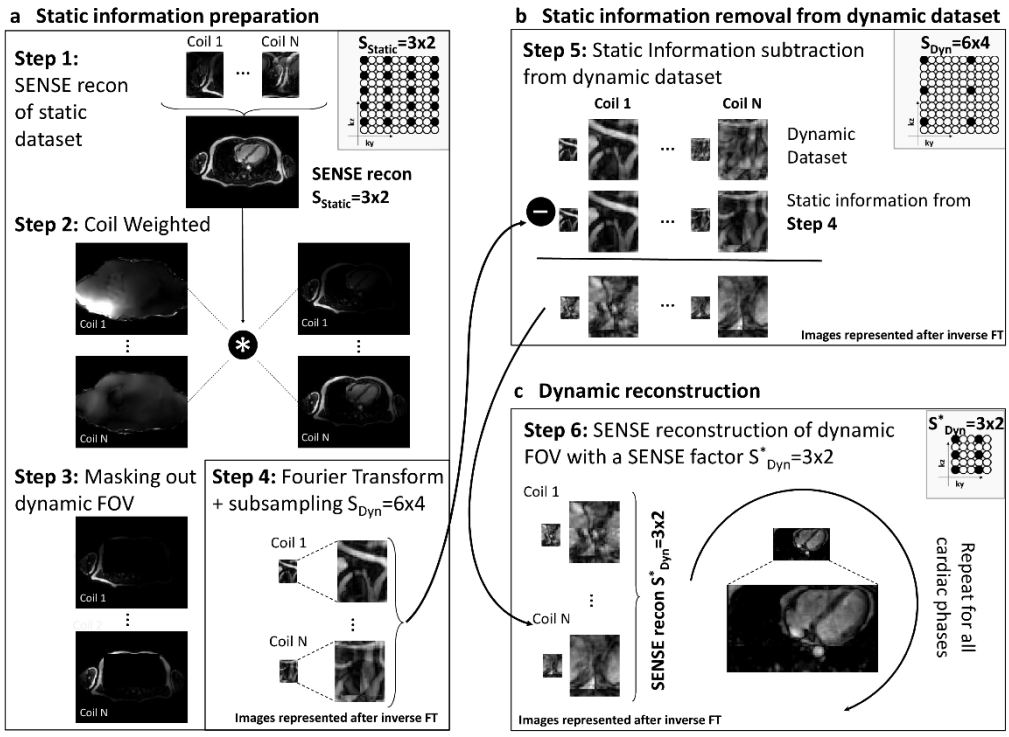

Supplemental Figure 3. Definition of the dynamic FOV mask. Steps needed to obtain the dynamic FOV mask. **a)** The procedure begins with Fourier transformation of the dynamic dataset in the temporal domain. **b)** Positive and negative datasets are reconstructed using conventional SENSE with an acceleration factor S_{Dyn} (the modulus for both datasets is shown for better visualization). **c)** Moduli for the positive and negative frequency components are added, and **d)** the result is segmented to generate the mask.

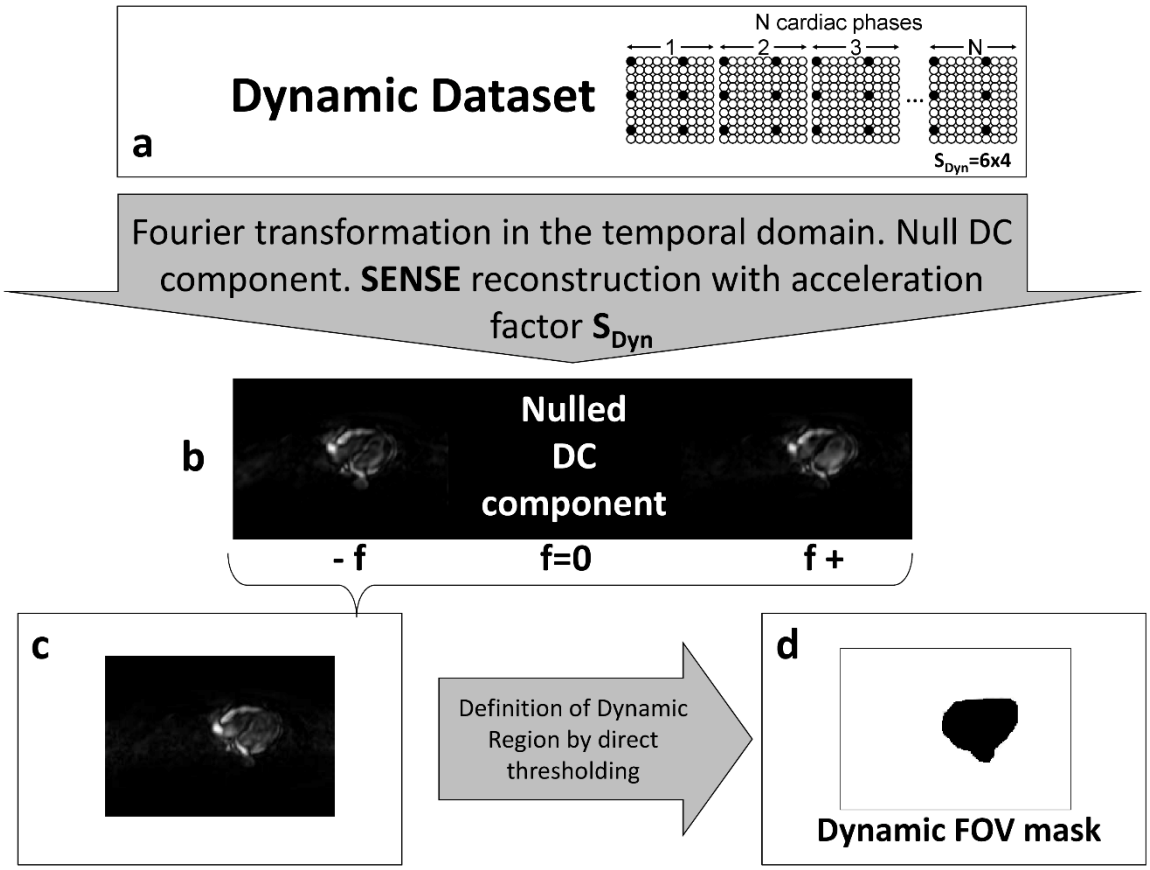

Supplemental Figure 4. Full sampled reconstruction (a) and simulated SENSE (b) and ESSOS (c) reconstructions with different acceleration factors D, from a single, fully sampled 2D cardiac cine acquired dataset. For panel b and c, the left column shows the magnitude images, the middle column shows the absolute error between each accelerated image and the fully sampled image and left column shows the g-maps. Images for left and middle panel for SENSE and ESSOS are scaled equally between them and g-maps are scaled between 0 and 8 in all cases. The rows indicate the results for different acceleration factors for both reconstructions.

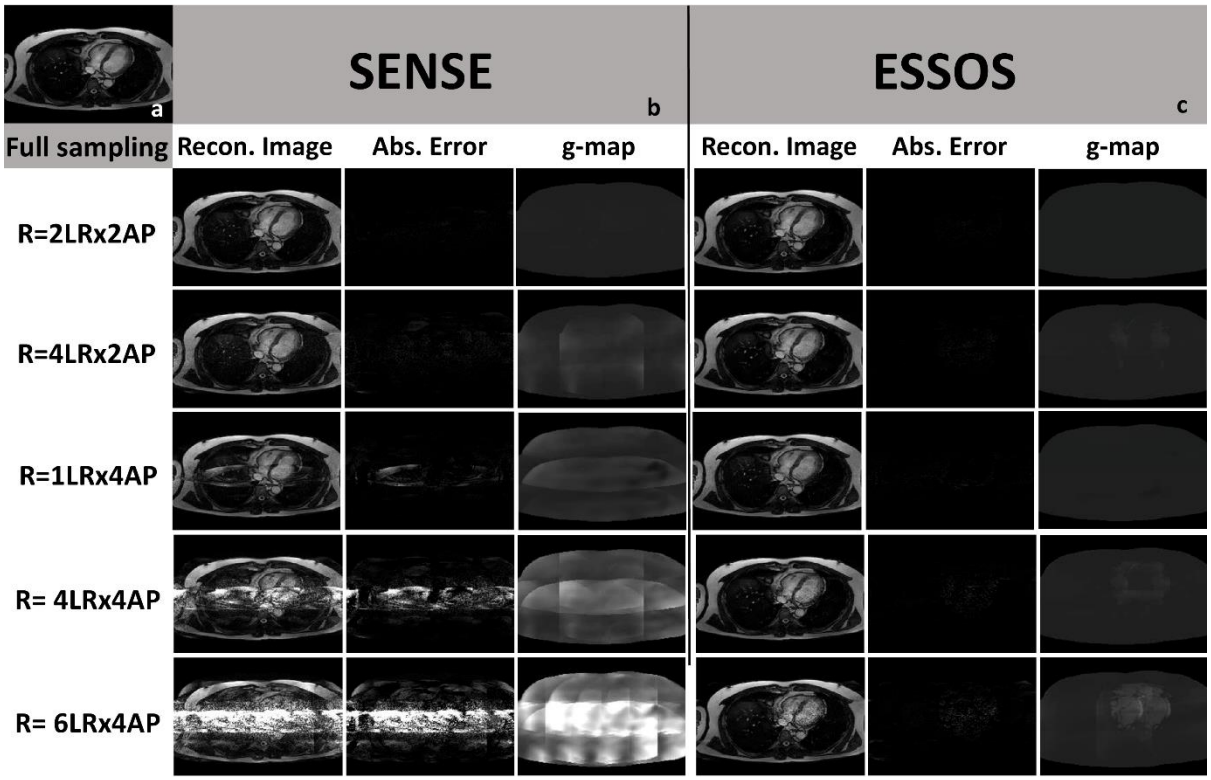

Supplemental Figure 5. Comparisons between 2D and 3D CMR measurements of ventricular volumes and mass.

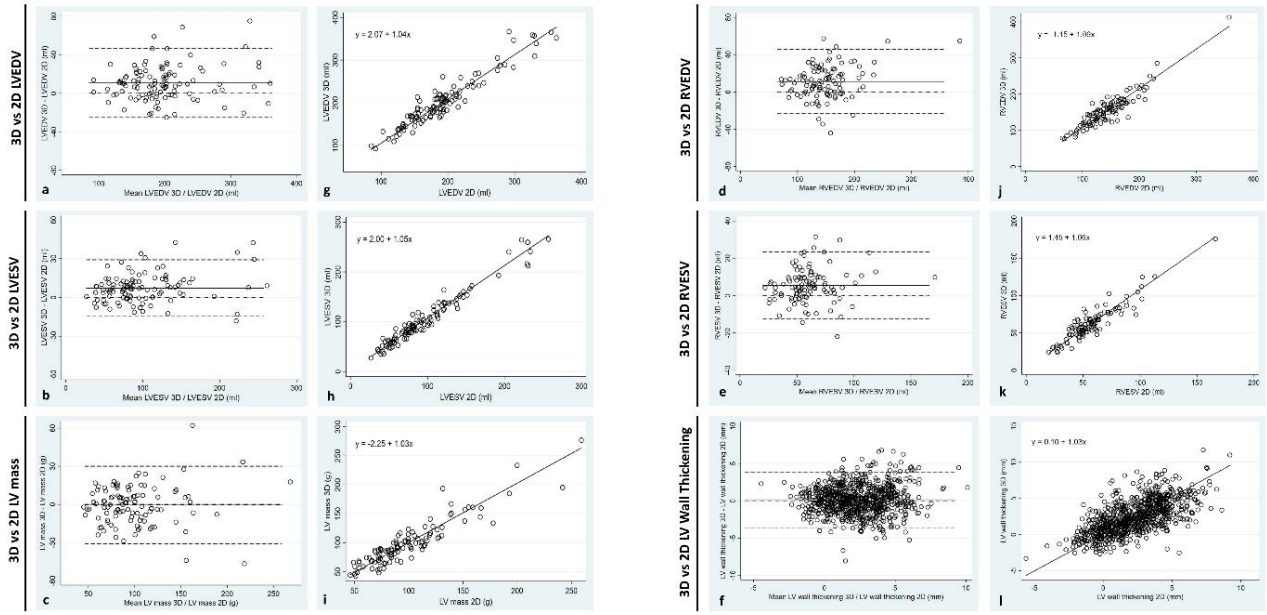

Bland-Altman plot (a, b, c, d, e, f) and Passing-Bablok regression (g, h, i, j, k) for comparisons between 2D and 3D CMR measurements Left Ventricle End Diastolic Volume (LVEDV), Left Ventricle End Systolic Volume (LVESV), Left Ventricle mass (LV mass), Right Ventricle End Diastolic Volume (RVEDV), Right Ventricle End Systolic Volume (RVESV) and LV Wall Thickening.

Reference (x axis), 2D measurements. Comparison method (y axis), 3D measurements.

Supplemental Figure 6. Example cases of different IQ visual assessment levels reported by an expert cardiologist for cine images (a, b, c) and 3D LGE images (d, e, f). Images were scored in Regular, Good and Very Good Image Quality (IQ).

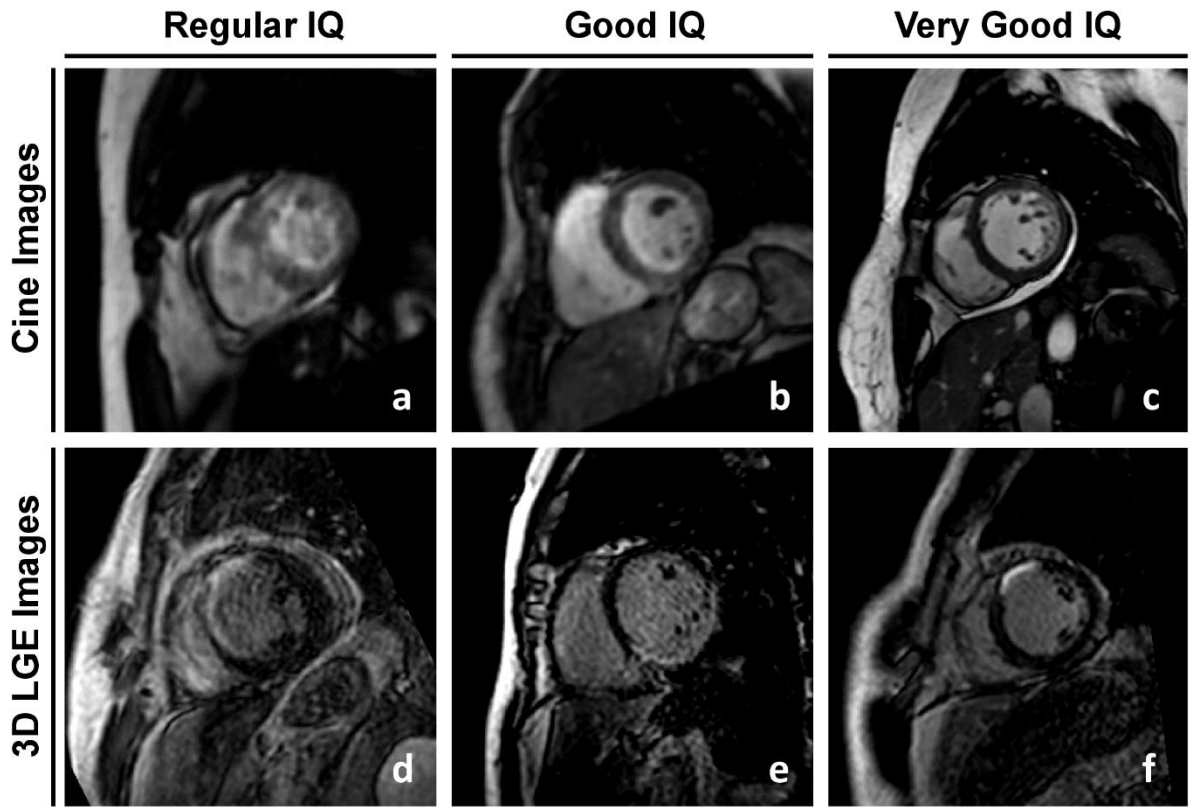

Supplemental Figure 7. Example case of ESSOS acquisition without intravenous contrast administration in a) diastolic and b) systolic cardiac phases.

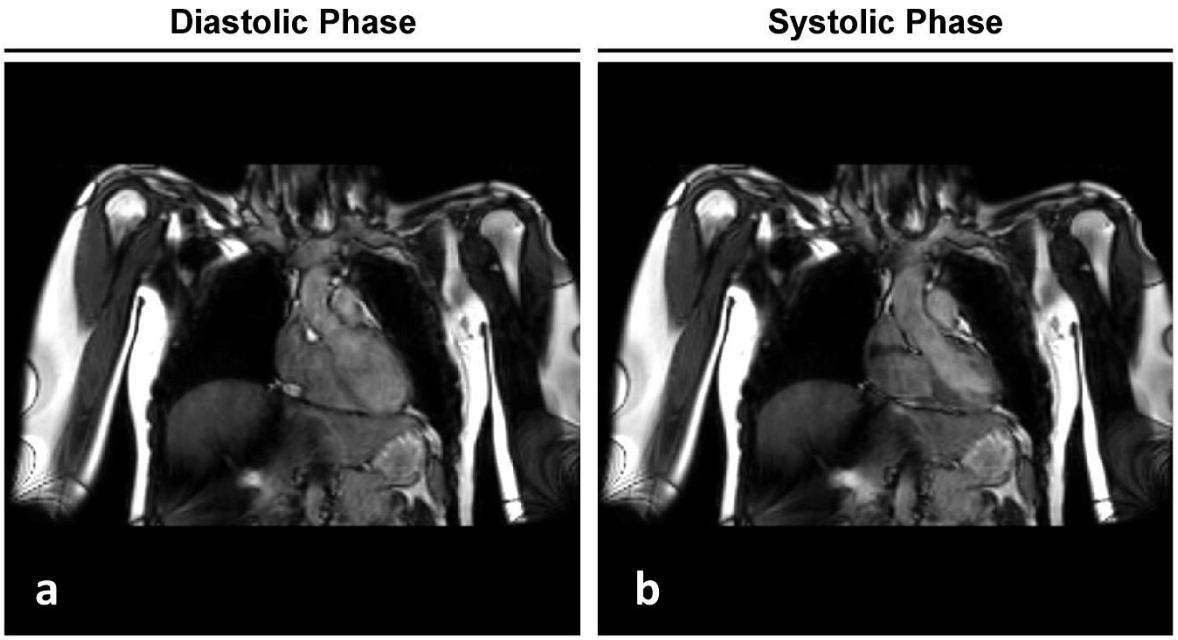

SUPPLEMENTAL TABLES

Supplemental Table 1. Absolute-agreement and consistency-of-agreement intraclass correlation coefficients (ICC) and their 95% confidence intervals (95%CI) for intra-observer comparisons for 3D CINE measurements.

Measured variable	n	Intraclass correlation coefficient (ICC)	
		Absolute agreement (95% CI)	Consistency of agreement (95% CI)
LVEF, %	20	0.99 (0.97 to 0.99)	0.99 (0.97 to >0.99)
LVEDV, mL	20	0.99 (0.98 to >0.99)	0.99 (0.98 to >0.99)
LVESV, mL	20	0.99 (0.99 to >0.99)	0.99 (0.99 to >0.99)
LV mass, g	20	0.89 (0.75 to 0.95)	0.90 (0.76 to 0.96)
RVEF, %	20	0.90 (0.77 to 0.96)	0.90 (0.77 to 0.96)
RVEDV, mL	20	0.93 (0.83 to 0.97)	0.94 (0.86 to 0.98)
RVESV, mL	20	0.93 (0.82 to 0.97)	0.94 (0.86 to 0.98)

ICC values ≥0.995 are indicated as >0.99, not rounded to 1.00

Supplemental Table 2. Bias and lower and upper limits of agreement from Bland-Altman plots and their 95% confidence intervals (95%CI) for intra-observer comparisons for 3D CINE measurements

Measured variable	n	Obs1-CMR	Obs1bis-CMR	Bland-Altman plot		
		Mean (SD)	Mean (SD)	Bias (95%CI)	Lower limit of agreement (95%CI)	Upper limit of agreement (95%CI)
LVEF, %	20	50.5 (11.4)	49.8 (11.2)	-0.7 (-1.5 to 0.1)	-4.1 (-5.5 to -2.7)	2.8 (1.3 to 4.2)
LVEDV, mL	20	219.1 (76.7)	219.4 (75.0)	0.3 (-4.7 to 5.3)	-20.5 (-29.1 to -11.9)	21.1 (12.5 to 29.7)
LVESV, mL	20	113.1 (60.6)	114.6 (59.6)	1.6 (-1.5 to 4.6)	-11.2 (-16.4 to -5.9)	14.3 (9.0 to 19.5)
LV mass, g	20	105.7 (37.4)	100.8 (29.0)	-4.9 (-12.1 to 2.3)	-34.9 (-47.4 to -22.5)	25.1 (12.7 to 37.6)
RVEF, %	20	58.2 (4.2)	58.5 (3.7)	0.3 (-0.5 to 1.1)	-3.2 (-4.6 to -1.7)	3.7 (2.3 to 5.2)
RVEDV, mL	20	155.5 (33.0)	150.4 (32.3)	-5.0 (-10.3 to 0.2)	-27.0 (-36.1 to -17.9)	17.0 (7.9 to 26.1)
RVESV, mL	20	65.0 (15.9)	62.5 (15.2)	-2.5 (-5.0 to 0.0)	-13.1 (-17.4 to -8.7)	8.0 (3.7 to 12.4)

Obs1, first measurement performed by Observer 1 (reference); Obs1bis, second measurement performed by Observer 1.

Supplemental Table 3. Absolute-agreement and consistency-of-agreement intraclass correlation coefficients (ICC) and their 95% confidence intervals (95%CI) for inter-observer comparisons for 3D CINE measurements

Measured variable	n	Intraclass correlation coefficient (ICC)	
		Absolute agreement (95%CI)	**Consistency of agreement (95%CI)**
LVEF, %	20	0.97 (0.94 to 0.99)	0.97 (0.93 to 0.99)
LVEDV, mL	20	0.99 (0.97 to >0.99)	0.99 (0.97 to >0.99)
LVESV, mL	20	0.99 (0.98 to >0.99)	0.99 (0.98 to >0.99)
LV mass, g	20	0.91 (0.79 to 0.96)	0.91 (0.79 to 0.96)
RVEF, %	20	0.61 (0.24 to 0.83)	0.65 (0.30 to 0.85)
RVEDV, mL	20	0.88 (0.73 to 0.95)	0.89 (0.75 to 0.96)
RVESV, mL	20	0.88 (0.72 to 0.95)	0.88 (0.71 to 0.95)

ICC values ≥0.995 are indicated as >0.99, not rounded to 1.00

Supplemental Table 4. Bias and lower and upper limits of agreement from the Bland-Altman plots and their 95% confidence intervals (95%CI) for inter-observer comparisons for 3D CINE measurements

Measured variable	n	Obs1-CMR	Obs2-CMR	Bland-Altman plot		
		Mean (SD)	Mean (SD)	Bias (95%CI)	Lower limit of agreement (95%CI)	Upper limit of agreement (95%CI)
LVEF, %	20	50.5 (11.4)	50.3 (11.3)	-0.2 (-1.4 to 1.1)	-5.3 (-7.5 to -3.2)	5.0 (2.9 to 7.1)
LVEDV, mL	20	219.1 (76.7)	219.4 (79.3)	0.3 (-5.4 to 6.0)	-23.6 (-33.5 to -13.7)	24.2 (14.3 to 34.1)
LVESV, mL	20	113.1 (60.6)	113.4 (60.5)	0.3 (-3.3 to 3.9)	-14.7 (-21.0 to -8.5)	15.4 (9.2 to 21.7)
LV mass, g	20	105.7 (37.4)	101.7 (32.1)	-4.0 (-10.8 to 2.8)	-32.6 (-44.4 to -20.7)	24.6 (12.8 to 36.4)
RVEF, %	20	58.2 (4.2)	56.1 (6.0)	-2.1 (-4.1 to -0.1)	-10.6 (-14.1 to -7.1)	6.4 (2.9 to 9.9)
RVEDV, mL	20	155.5 (33.0)	149.9 (30.9)	-5.6 (-12.5 to 1.4)	-34.7 (-46.8 to -22.7)	23.6 (11.6 to 35.7)
RVESV, mL	20	65.0 (15.9)	66.0 (17.0)	1.0 (-2.8 to 4.8)	-15.1 (-21.7 to -8.4)	17.1 (10.4 to 23.7)

Obs1, first measurement performed by Observer 1 (reference); Obs2, measurement performed by Observer 2.

Supplemental Table 5. Absolute-agreement and consistency-of-agreement intraclass correlation coefficients (ICC) and their 95% confidence intervals (95%CI) from the intra- and inter-observer comparisons of 3D late gadolinium contrast-enhanced myocardial mass (% of left ventricle)

	n	Intraclass correlation coefficient (ICC)	
		Absolute agreement (95%CI)	**Consistency of agreement (95%CI)**
Intra-observer	20	0.97 (0.92 to 0.99)	0.97 (0.93 to 0.99)
Inter-observer	20	0.92 (0.80 to 0.97)	0.91 (0.80 to 0.97)

Supplemental Table 6. Bias and lower and upper limit of agreement from the Bland-Altman plots and their 95% confidence intervals (95%CI) for intra- and inter-observer comparisons of 3D late gadolinium contrast-enhanced myocardial mass (% of left ventricle)

	n	Obs1-CMR	Obs1bis-CMR	Obs2-CMR	Bland-Altman plot		
		Mean (SD)	Mean (SD)	Mean (SD)	Bias (95%CI)	Lower limit of agreement (95%CI)	Upper limit of agreement (95%CI)
Intra-observer	20	16.9 (10.2)	17.8 (10.2)	-	0.8 (-0.3 to 2.0)	-4.0 (-5.9 to -2.0)	5.6 (3.6 to 7.6)
Inter-observer	20	16.9 (10.2)	-	16.1 (10.7)	-0.9 (-2.9 to 1.2)	-9.3 (-12.9 to -5.8)	7.6 (4.1 to 11.2)

LGE, late gadolinium contrast-enhanced; LV: left ventricle.

Obs1, first measurement performed by Observer 1 (reference); Obs1bis, second measurement performed by Observer 1; Obs2, measurement performed by Observer 2.

Supplemental Video 1. Representation of CENTRAL (Spiral) k-space filling along different cardiac phases for dynamic dataset used for ESSOS.

Supplemental Video 2. Example case from patient undergoing 3D ultrafast protocol-only. The images present short axis MPR for 3D cine (left) and 3D LGE (right).

Supplemental Video 3. Example case from patient undergoing 3D ultrafast protocol-only. The images present short axis MPR for 3D cine (left) and 3D LGE (right).

Supplemental Video 4. 4CH 2D cine and 4CH MPR for 3D isotropic cine acquisition of patient with altered cardiac contractibility

Supplemental Video 5. Short Axis 2D cine and short axis MPR for 3D isotropic cine acquisition of patient with altered cardiac contractibility

Supplemental Video 6. 4CH 2D cine and 4CH MPR for 3D isotropic cine acquisition of patient with preserved cardiac contractibility

Supplemental Video 7. Short Axis 2D cine and short axis MPR for 3D isotropic cine acquisition of patient with preserved cardiac contractibility

SUPPLEMENTAL REFERENCES

1. Fuderer M, van den Brink J, Jurrissen M. SENSE reconstruction using feed forward regularization. Proc Int Soc Magn Reson Med 2004;11.

2. Koo TK, Li MY. A Guideline of Selecting and Reporting Intraclass Correlation Coefficients for Reliability Research. J Chiropr Med 2016;15:155-63.

3. Bland JM, Altman DG. Statistical methods for assessing agreement between two methods of clinical measurement. Lancet 1986;1:307-10.

4. Passing H, Bablok. A new biometrical procedure for testing the equality of measurements from two different analytical methods. Application of linear regression procedures for method comparison studies in clinical chemistry, Part I. J Clin Chem Clin Biochem 1983;21:709-20.

5. Lin LI. A concordance correlation coefficient to evaluate reproducibility. Biometrics 1989;45:255-68.